

Regulating the Interfacial Electron Density of $\text{La}_{0.8}\text{Sr}_{0.2}\text{Mn}_{0.5}\text{Co}_{0.5}\text{O}_3/\text{RuO}_x$ for Efficient and Low-Cost Bifunctional Oxygen Electrocatalysts and Rechargeable Zn-air Batteries

Yawen Dai¹, Jie Yu^{1,*}, Zhenbao Zhang¹, Shuo Zhai¹, Chun Cheng¹, Siyuan Zhao¹, Peng Tan²,
Zongping Shao³, Meng Ni^{1,*}

¹Department of Building and Real Estate, Research Institute for Sustainable Urban Development (RISUD) and Research Institute for Smart Energy (RISE), The Hong Kong Polytechnic University, Hung Hom, Kowloon, Hong Kong, P. R. China.

²Department of Thermal Science and Energy Engineering, University of Science and Technology of China, Hefei 230026, Anhui, P. R. China.

³State Key Laboratory of Materials-Oriented Chemical Engineering, College of Chemical Engineering, Nanjing Tech University, No. 5 Xin Mofan Road, Nanjing 210009, P. R. China

*Corresponding authors

E-mail addresses: yujie19920114@njtech.edu.cn (Jie Yu); meng.ni@polyu.edu.hk (Meng Ni)

Abstract

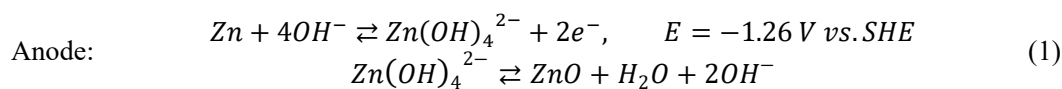
$\text{La}_{0.8}\text{Sr}_{0.2}\text{Mn}_{0.5}\text{Co}_{0.5}\text{O}_3$ (LSMC) perovskite anchored with RuO_x (LSMC-Ru) is fabricated as a new bifunctional electrocatalyst, with low dosage (2.43 wt%) and high utilization of noble metal Ru. The LSMC-Ru exhibits outstanding bifunctional activity with a low potential gap of 0.72 V between the oxygen evolution reaction (OER) potential at 10 mA cm^{-2} and the oxygen reduction reaction (ORR) half-wave potential. The strong electronic interaction between RuO_x and LSMC is confirmed by both experiments and theoretical calculations. Consequently, the electron-rich Mn centers promote ORR while the electron-deficient Ru centers facilitate OER. A Zn-air battery using the LSMC-Ru air electrode delivers a peak power density of 159 mW cm^{-2} and a low charge-discharge potential gap of 0.58 V at 2 mA cm^{-2} . The high round-trip energy efficiency of 60.6% is retained after 300 cycles. This strategy of anchoring low dosage noble metal catalyst to perovskite can be extended to other systems of noble metal-nonnoble metal composite electrocatalysts to achieve both competitive performance and low cost.

Keywords: oxygen reduction reaction, oxygen evolution reaction, perovskite oxide, Zn-air battery, electronic structure regulation

1. Introduction

To meet the increasing energy demand of the modern society, sustainable and efficient energy conversion and storage technologies have been rapidly developed.^{1,2} The rechargeable Zn-air battery (ZAB) is one of the most promising technologies for the next-generation energy storage system, mainly due to the high theoretical energy density (1086 Wh kg^{-1}), the abundant resource and nontoxic feature of Zn, as well as the high safety of aqueous electrolytes.^{3,4} However, the practical implementation of

rechargeable ZABs is still impeded by the poor durability and unsatisfactory performance. The charge and discharge of ZABs are based on the following electrochemistry:⁵



The poor durability of rechargeable ZABs is mainly caused by the Zn dendrite formation and growth as well as the passivation of Zn electrode.⁶ The unsatisfactory performance of ZABs is mainly due to the sluggish oxygen reduction reaction (ORR) and oxygen evolution reaction (OER) at the air electrode, which in turn causes high charge voltage (i.e. over 2.0V), low discharge voltage (i.e. 1.2V), and thus low round-trip energy efficiencies (< 60%).⁷⁻⁹ Currently, the noble metals are used in benchmark electrocatalysts for OER (IrO₂ and RuO₂) and ORR (Pt/C), delivering the relatively low potential gap (ΔE) of about 0.7 V between OER ($j=10 \text{ mA cm}^{-2}$) and ORR half wave potential. However, the high catalyst cost of noble metals hinders the wide application. Although some nonnoble metal electrocatalysts have been developed, they still have lower activity than noble metals.¹⁰ For example, transition metal oxides such as spinel and perovskites always show ΔE of 0.8~1 V.^{8,11} Therefore, it is important to develop bifunctional OER/ORR electrocatalysts with high activity and low cost for the development of high performance and low-cost ZABs, but it is still challenging.

In addition to the development of novel noble metal-free electrocatalysts, another promising strategy is to combine non-noble metals and noble metals with low dosage (high utilization) to achieve both high activity and low cost. In these electrocatalysts, the interaction between different metals can regulate the electronic structure of electrocatalysts, which in turn can affect the electrocatalytic activity. An in-depth understanding on these interactions is critical for designing electrocatalysts for ZABs. For example, Shao's group integrated Pt/C with a Sr(Co_{0.8}Fe_{0.2})_{0.95}P_{0.05}O_{3- δ} perovskite oxide by a facile ball milling method, realizing good bifunctional activity with ΔE of 0.73 V using a Pt/perovskite

weight ratio of 1/2.¹² Besides, doping is a commonly used method for combining noble metals with non-noble metals. For example, noble metal Ir was introduced into the B-site of perovskite structure by doping to form SrIrO₃ and SrZr_xIr_{1-x}O₃, which achieved higher OER activity (overpotential of 240 mV at a current density of 10 mA cm⁻²) with lower Ir content (40 wt%) than the benchmark IrO₂.^{13,14} Similarly, a Ru-doped LaCoO₃ perovskite was synthesized and applied as the electrocatalysts for ZABs, which delivered decent bifunctional OER/ORR activity and battery performance.¹⁵ However, doping may cause the noble metals to distribute throughout the entire bulk material, and thus the exposure and utilization of noble metals are both low. It can be seen from the above-mentioned literature that the dosage of the noble metal is still high (i.e. 33 wt% in ref. 12, 40 wt% in ref. 13, and 58 wt% in ref. 14). For comparison, surface anchoring could be a better method to load low-dosage noble metals on the surface of nonnoble metals. In this way, the non-noble metal oxides could act as a support for the noble metals, thus preventing the aggregation of active sites and improving the utilization of noble metals.^{16,17} Lv *et al.* deposited Pt nanoparticles on LiTiO₂ surface by solvothermal reduction method, and the obtained material showed better ORR activity ($E_{1/2}=0.92$ V vs. RHE) than that of the benchmark Pt/C.¹⁸ The above works adequately demonstrate the superiority of the noble metal-non-noble metal combining strategy.

Among the non-noble metal materials, perovskite oxides have attracted much research interests due to their relatively high ionic/electronic conductivity, abundance on earth, and high compositional flexibility, which offer large opportunities to regulate the electronic structure.¹⁹⁻²¹ Great advances have been made in recent years to exploit perovskite-based OER and ORR electrocatalyst. For example, La_{0.8}Sr_{0.2}Mn_{0.5}Co_{0.5}O₃ (LSMC) showed good electrocatalytic activity, consistent with the ORR/OER volcano plots reported by Shao-Horn's group. Recent research on A-site and B-site substitution of LSMC also demonstrated improved activity.²²⁻²⁴ For noble metal materials, Ru is attractive due to its high intrinsic activity for OER and the lowest price in the noble metal family.²⁵ Therefore, anchoring Ru species on the surface of perovskite oxides is expected to be a promising strategy for electrocatalyst development. However, the report on the Ru species-anchored perovskite oxides is very limited,

especially for aqueous bifunctional OER/ORR. The RuO_x-perovskite oxide interaction and the mechanism of the performance regulation are also unclear.

Therefore, LSMC perovskite anchored with ultrafine RuO_x (LSMC-Ru) is designed as an efficient bifunctional OER/ORR electrocatalyst for ZABs. The material properties of the developed LSMC-Ru electrocatalyst are systematically characterized by various characterization techniques. The bifunctional activity of LSMC-Ru catalyst towards ORR and OER is obtained by electrochemical tests. To gain a fundamental understanding of the interaction between RuO_x and LSMC, atomic level calculations based on density functional theory (DFT) are conducted. LSMC-Ru is applied to fabricate the air electrode of ZAB, which achieves a low charge-discharge potential gap of 0.58 V at 2 mA cm⁻² and a peak power density of 159 mW cm⁻². The excellent activity of LSMC-Ru with very low dosage (2.43 wt%) of Ru demonstrates the potential of this strategy for developing high performance and low-cost electrocatalyst for OER/ORR.

2. Results and discussion

2.1 Composition and structure characterization

LSMC was synthesized by the conventional sol-gel method. LSMC-Ru was obtained by a facile solution treatment of LSMC in RuCl₃ followed by annealing. The detailed procedure is described in the supporting formation (**Figure S1**). The synthesis condition of the Ru species anchored LSMC was varied by changing the concentration of RuCl₃ solution and the annealing temperature. The electrocatalytic activities of the materials prepared under various conditions are evaluated by the electrochemical linear scan voltammetry (LSV) tests to identify the optimal synthesis conditions (RuCl₃ solution concentration and annealing temperature). It is seen that the optimal synthesis condition is 1.5 mg mL⁻¹ RuCl₃ and 200 °C annealing (**Figure S2**). The LSMC-1.5 mg mL⁻¹ Ru and LSMC-1.5 mg mL⁻¹ Ru-200 samples keep nearly the same X-ray diffraction (XRD) peaks with the bare LSMC, indicating that the crystal structure of the LSMC is preserved, and the surface Ru species has a rather low crystallinity (**Figure S3**). In comparison, the 300 and 400 °C-annealed samples display

obvious peaks of crystalline RuO₂, implying the aggregation of Ru species, which leads to the decreased electrocatalytic activity as compared to the 200 °C-annealed sample (**Figure S2b and S2d**). Accordingly, the highest-performance sample of LSMC-1.5 mg mL⁻¹ Ru-200 is named as LSMC-Ru in the following discussion. The Rietveld XRD results (**Figure 1a and 1b**) show that the LSMC phase has a rhombohedral structure with an R-3h space group. The bare LSMC has lattice parameters of a=b=5.47523 Å, and c=13.26093 Å. In comparison, the LSMC phase in LSMC-Ru has a slightly expanded lattice with a=b=5.47531 Å, and c=13.26291 Å, which is ascribed to the cation leaching during the Ru species anchoring process. In addition, the very weak peaks of tetragonal RuO₂ (110) at 27.9° and (101) at 35.1° can be identified in LSMC-Ru as labeled by the pink star in **Figure 1b**. Further characterizations are conducted to confirm the low dosage and high utilization of Ru. The mass ratio of the RuO₂ phase is 1.1 wt% from XRD, corresponding to the elemental Ru mass ratio of 0.84 wt%. The value is lower than that obtained from the inductively coupled plasma (ICP) test (Ru 2.43 wt%) (**Table S1**). The results suggest that some atomic or amorphous Ru-O clusters are anchored on the LSMC surface in addition to the crystalline RuO₂ detected by XRD. SEM images (**Figure S4a and S4b**) show that LSMC-Ru retains the original micromorphology of the bare LSMC. In the energy dispersive X-ray (EDX) spectra (**Figure S4c and S4d**), LSMC-Ru shows an obvious Ru signal in addition to the La, Sr, Mn Co composition inherited from LSMC, indicating the successful anchoring of Ru species on LSMC.

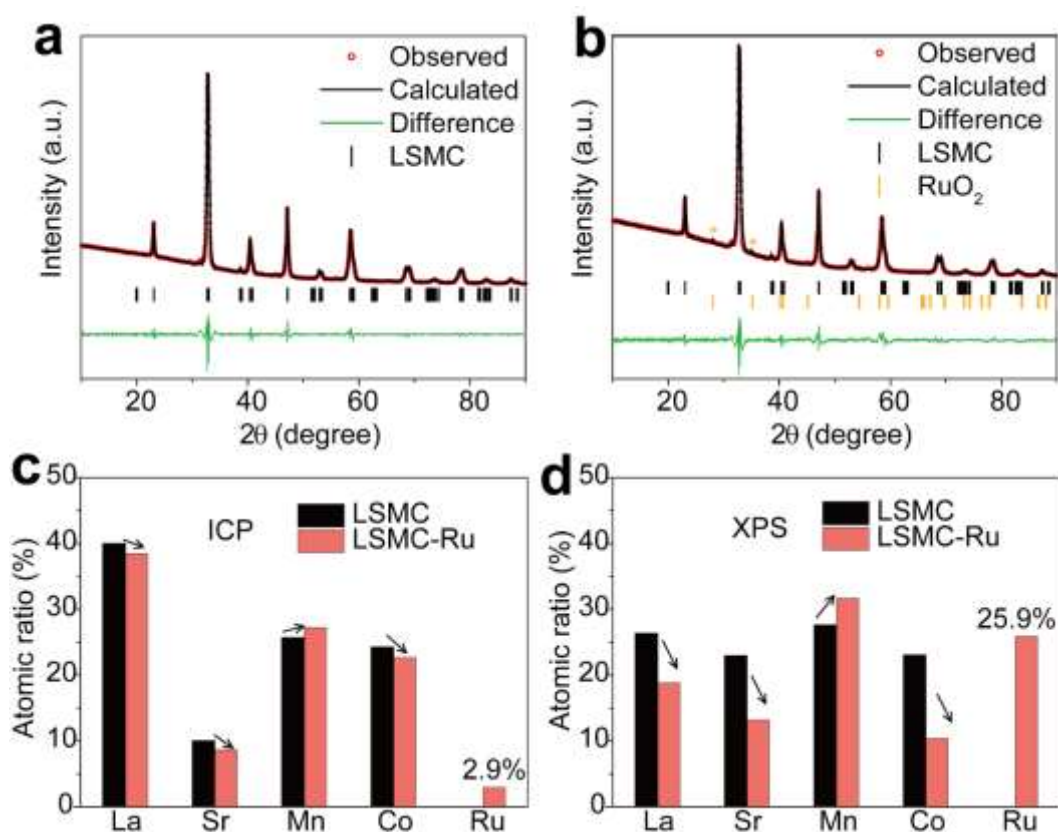


Figure 1. Rietveld refined powder XRD patterns of the (a) LSMC and (b) LSMC-Ru. The change of atomic metal ratio of LSMC and LSMC-Ru detected by (c) ICP and (d) XPS.

From the quantified results of EDX (**Figure S5**) and ICP (**Figure 1c**, **Table S1**), LSMC shows metal atomic ratios close to the chemical formula of $\text{La}_{0.8}\text{Sr}_{0.2}\text{Co}_{0.5}\text{Mn}_{0.5}\text{O}_3$. In comparison to the bare LSMC, LSMC-Ru shows decreased ratios in La, Sr, and Co but increased ratios of Mn and Ru (**Figure S5**, **Figure 1c**, and **Table S1**). Moreover, the ICP result of the filtered solution (the upper liquid in **Figure S1c**) of the Ru-anchoring process is presented in **Table S2**. Ru is not detectable in the filtered solution, indicating that Ru species is efficiently transferred from the solution phase to the solid phase during the Ru-anchoring process. Besides, the filtered solution shows relatively high contents of La (3.90 mmol L^{-1}), Sr (1.76 mmol L^{-1}), Co (3.72 mmol L^{-1}), but rather low content of Mn (0.03 mmol L^{-1}). Combining the above results, we conclude that La, Sr, and Co are selectively etched during the Ru anchoring process, whereas Mn is prone to be preserved. The quantified X-ray photoelectron spectroscopy (XPS) results (**Figure 1d**) further confirm the selective cation leaching during the Ru-

anchoring process, which leads to an Mn-rich and Ru-rich surface of LSMC-Ru. It should benefit the oxygen electrocatalysis since Mn is regarded as the ORR-active center whereas Ru is regarded as the OER-active center according to previous research²⁹⁻³². Furthermore, LSMC-Ru shows an entire Ru atomic ratio of 2.9 % (**Figure 1c**) and a surface Ru atomic ratio of 25.9 % (**Figure 1d**), which confirms the low dosage and high exposure (thus high utilization) of Ru on the surface.

The TEM image of the bare LSMC shows a particle size of several hundred nanometers (**Figure S6a**) and a smooth surface (**Figure 2a**). In comparison to LSMC, LSMC-Ru shows the similar particle size (**Figure S6b**), but a relatively rougher surface with ultrafine dark dots that could be assigned to Ru-species (**Figure 2b**). The HRTEM image (**Figure S6c**) clearly displays the lattice fringes with the d-spacing of 0.28 nm, which could be assigned to the (110) lattice plane of LSMC. In the HRTEM image of LSMC-Ru (**Figure 2c**), the lattice fringes with d-spacing of 0.19 nm corresponding to LSMC (024) plane and 0.25 nm corresponding to RuO₂ (101) plane are identified, and RuO₂ shows an ultrasmall size of about 1.5 nm. The lattice fringe of LSMC-Ru is not as clear as that of the bare LSMC, which is due to the cation etching leading to the reduced crystallinity near the surface region. **Figure 2d** shows the STEM image of LSMC-Ru and the corresponding EDX-mapping images. La, Sr, Mn, and Co are homogeneously distributed on the bulk material, whereas the distribution of Ru is enriched on the surface. The EDX spectrum of the surface region (**Figure S7**) shows the dominant composition of Mn and Ru, which is consistent with the XPS quantification (**Figure 1b**).

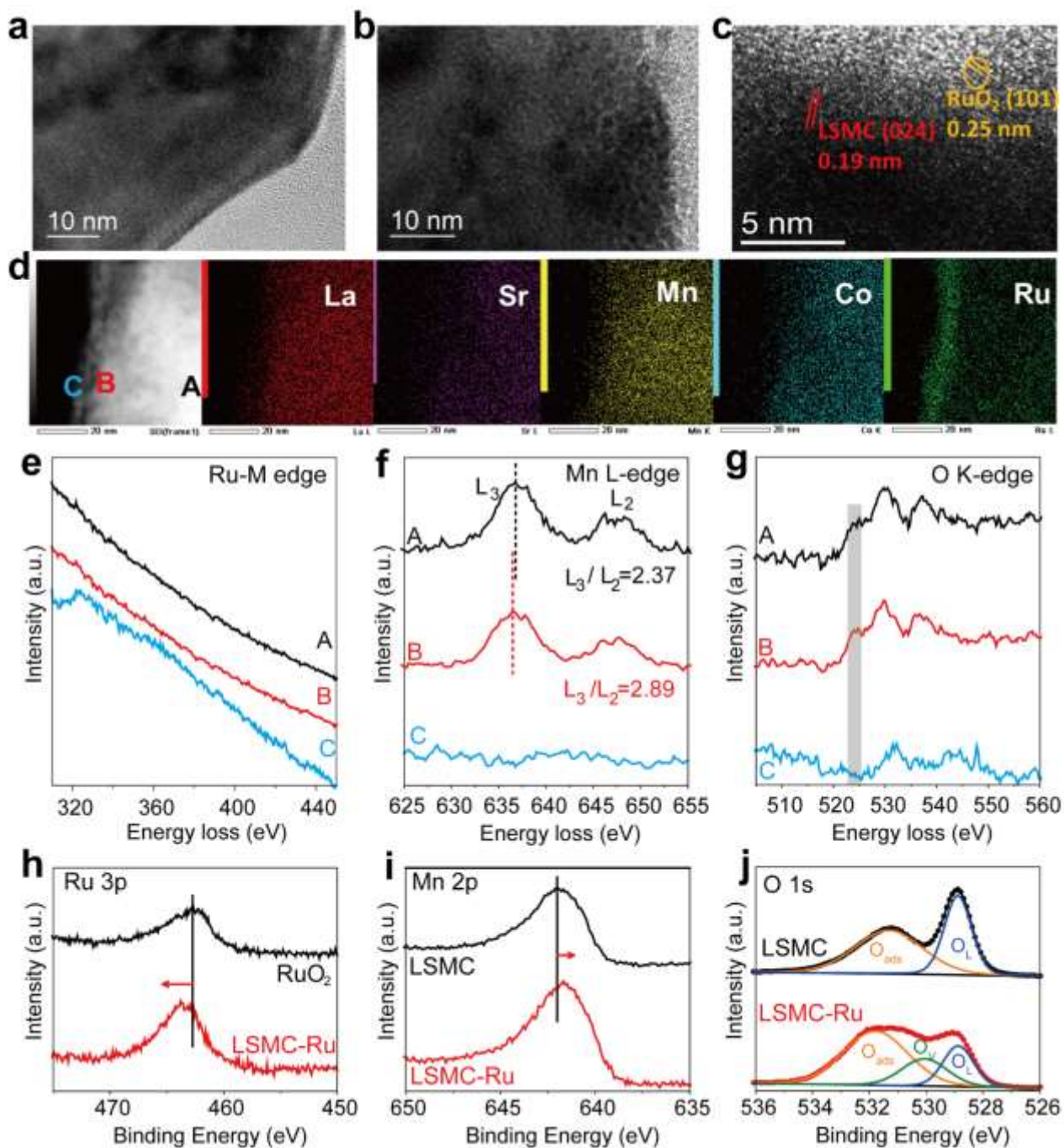


Figure 2. TEM images of (a) the bare LSMC and (b) LSMC-Ru. (c) The HRTEM image of LSMC-Ru. (d) STEM image and the corresponding EDX-mapping of LSMC-Ru. Spatially resolved EELS spectra of (e) Ru-M edge, (f) Mn-L edge, and (g) O-K edge of the regions labeled in (d). XPS spectra of (h) Ru 3p, (i) Mn 2p, and (j) O 1s of LSMC-Ru comparing with the single component LSMC and RuO₂.

2.2 The electronic interaction between RuO_x and LSMC

To get a further insight into the chemical environment of the LSMC-Ru heterostructure, electron

energy loss spectra (EELS) (**Figure 2e-2g**) and XPS spectra (**Figure 2h-2j**) are analyzed. We focus on the spectra of Mn, Ru, and O, because they are the dominant composition on the material surface and thus are responsible for the electrocatalytic reactions. As labeled in **Figure 2d**, the EELS spectra of the bulk-LSMC (region A), interface-LSMC (region B), and RuO_x (region C) are extracted. For Ru M-edge (**Figure 2e**), Ru signal is only observed in region C, and it disappears in region A and B, which is consistent with the EDX-mapping. For Mn-L edge (**Figure 2f**), the signal appears in region A and B but not in region C. Furthermore, region A shows a characteristic L₃/L₂ (ratio of integrated peak intensity) of 2.37, manifesting the Mn (III) valence state of the bulk-LSMC.³³ In comparison, region B shows a higher L₃/L₂ of 2.89, and the L₃ peak shifts to a lower energy loss value as compared to region A, indicating a mixed valence state of Mn (II/III).^{33,34} The lower Mn valence state of interface-LSMC than that of bulk-LSMC demonstrates the interfacial electron transfer from RuO_x to LSMC. For O-K edge (**Figure 2g**), the pre-peak (labeled by the grey square) appears in region A and B but disappears in region C, which implies the unsaturated oxygen coordination of Ru in RuO_x.³⁵

For XPS spectra, the change of the electronic structure of the metal sites can be inferred from the binding energy shifts.^{12,36,37} The binding energy of Ru 3p_{3/2} (**Figure 2h**) in LSMC-Ru shifts to a higher value (463.8 eV) as compared to that in the bare RuO₂ (462.7 eV), suggesting the decreased local electron density of Ru. The identical binding energy of Co 2p_{3/2} (780.0 eV) for the bare LSMC and LSMC-Ru (**Figure S8**) indicates that the Ru-decoration does not change the chemical environment of Co. In contrast, LSMC-Ru shows a lower binding energy of Mn 2p_{3/2} (641.6 eV) than the bare LSMC (642.0 eV) (**Figure 2i**), suggesting the increased local electron density of Mn. As a result, the electron-deficient Ru centers tend to accept electrons from the oxygen species in electrolyte and thus promote OER, and the electron-rich Mn centers tend to donate electrons to the oxygen species in electrolyte and thus promote ORR. The above analysis indicates that the strong interaction between the LSMC support and the surface anchored RuO_x leads to a favorable electronic structure for the bifunctional ORR and OER electrocatalysis. Additionally, the O 1s spectra (**Figure 2j**) can be deconvoluted into three peaks representing the adsorbed oxygen (O_{abs}), lattice oxygen (O_L), and oxygen vacancy (O_V).³⁸

LSMC-Ru shows more oxygen vacancies than the bare LSMC, which is a beneficial feature for oxygen electrocatalysis.³⁹

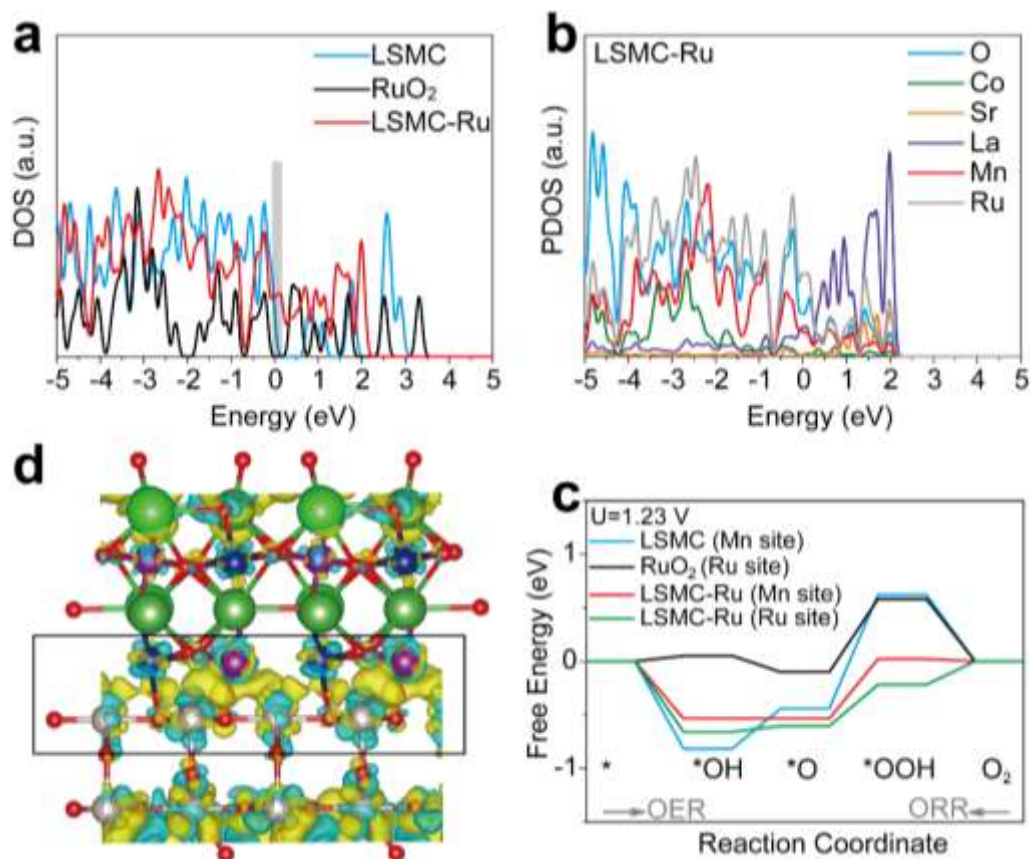


Figure 3. DFT calculation. (a) Total DOS of LSMC, RuO₂, and LSMC-Ru. (b) PDOS of LSMC-Ru. (c) Differential charge density of LSMC-Ru. The red, grey, purple, green, light blue, and dark blue balls represent O, Ru, Mn, La, Sr, Co, respectively. The yellow and blue clouds represent electron accumulation and electron depletion, respectively. (d) Free Energy diagrams at 1.23 V.

To further verify the above analysis, density functional theory (DFT)-based theoretical calculations are conducted to gain in-depth understanding of the electronic interaction between RuO_x and LSMC and its effect on the OER/ORR. The model (**Figure S9**) is constructed according to the experimentally-obtained crystal structure and atom ratio. The results of density of states (DOS) (**Figure 3a**) show that LSMC-Ru has continuous DOS around the Fermi level with zero bandgap, indicating the metallic characteristic of the heterostructure interface, which guarantees the fast electron

transfer.⁴⁰ Besides, the higher DOS of LSMC-Ru than that of the bare LSMC and RuO₂ at Fermi level indicates the increased electron mobility of the heterostructure.⁴¹ The projected DOS (PDOS) of Mn and Ru matches well (**Figure 3b**), which induces the strong electronic coupling.⁴² As a result, the electron density is redistributed at the heterostructure interface as shown by the differential charge density (**Figure 3c**). At the interface region, electron depletion around Ru and electron accumulation around the Mn-O bond is clearly observed, which is consistent with the experimental XPS and EELS analysis. Detailed Bader charge calculation indicates the 0.45 e⁻ interfacial electron transfer from RuO_x to LSMC for the heterostructure model. The Gibbs free energy diagrams (**Figure 3d**) show that this heterostructure effectively lowers the reaction energy barrier. The Ru site and Mn site of LSMC-Ru show the highest OER and ORR activity, respectively. For OER, the heterostructure significantly accelerates the rate-determining-step of O-O bond formation and stabilizes *OOH species, resulting in a low energy barrier of 0.39 eV. For ORR, the heterostructure greatly promotes the steps of O₂ adsorption and *OH desorption, and thus leads to the low energy barrier of 0.53 eV. The DFT calculation validates the regulated interfacial electron density between LSMC and RuO_x, and predicts the outstanding intrinsic OER/ORR activity of the LSMC-Ru heterostructure.

2.3 The bifunctional oxygen electrocatalytic performance

The bifunctional oxygen electrocatalytic activity and stability of the synthesized materials are evaluated on rotating disk electrode (RDE). As indicated by the LSV curves of the ORR (**Figure 4a**), LSMC-Ru realizes high activity with a half-wave potential ($E_{\text{ORR}, 1/2}$) of 0.76 V vs. RHE, which is a significant improvement compared with the bare LSMC (0.60 V vs. RHE) and RuO₂ (0.55 V vs. RHE). The $E_{\text{ORR}, 1/2}$ of LSMC-Ru is 80 mV more negative than the commercial state-of-the-art 20 wt % Pt/C (0.84 V vs. RHE). Moreover, LSMC-Ru and Pt/C show the same limiting ORR current density of 5.2 mA cm⁻². The electron transfer number calculated from the K-L equation is 4.02 for Pt/C and 3.84 for LSMC-Ru (**Figure S10**), implying that the four-electron reduction process is favored for the ORR. Meanwhile, the Tafel slope (**Figure 4b**) of LSMC-Ru has the lowest value of 56.0 mV dec⁻¹ among all

the tested samples ($154.6 \text{ mV dec}^{-1}$ for LSMC, $227.2 \text{ mV dec}^{-1}$ for RuO_2 , and 78.5 mV dec^{-1} for Pt/C), which demonstrates the superior ORR kinetics of LSMC-Ru. Chronoamperometric measurement at 0.30 V vs. RHE (**Figure 4c**) shows that LSMC-Ru retains 92% of the initial ORR current density after the 16 h test, which is much more stable than Pt/C with only 75% retention.

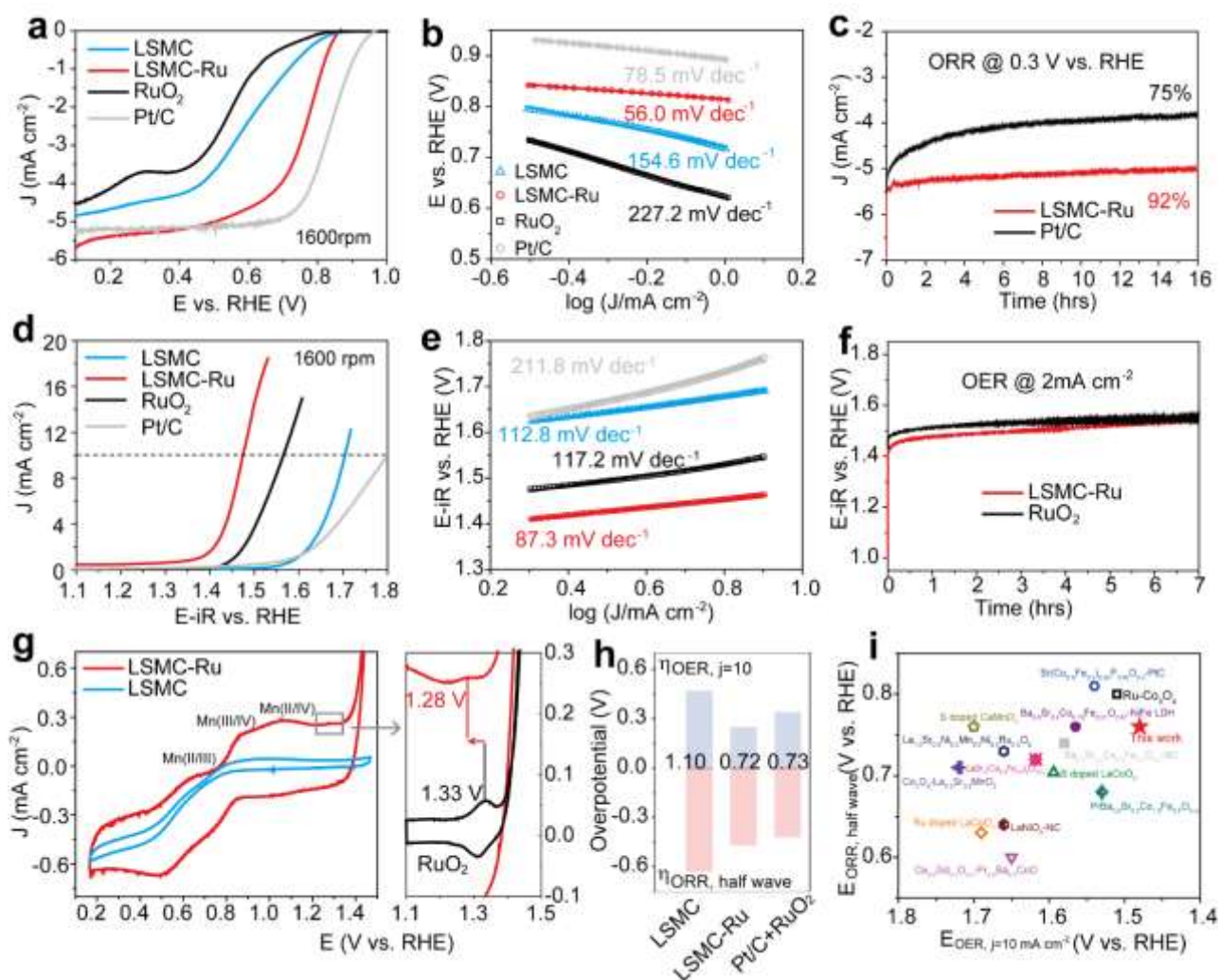


Figure 4. (a) LSV curves of ORR at the scan rate of 5 mV s^{-1} in O_2 saturated 0.1 M KOH and (b) the corresponding Tafel plots. (c) Chronoamperometric response of ORR durability at 0.30 V vs. RHE. (d) LSV curves of OER at the scan rate of 5 mV s^{-1} in O_2 saturated 0.1 M KOH and (e) the corresponding Tafel plots. (f) Chronopotentiometry response of OER durability at 2 mA cm^{-2} . (g) Cyclic voltammograms at the scan rate of 5 mV s^{-1} in N_2 saturated 0.1 M KOH . (h) The potential gap (ΔE) between OER ($j=10 \text{ mA cm}^{-2}$) and ORR half-wave potential. (i) A comparison of the OER and ORR

bifunctional activity of LSMC-Ru in this work with other recently reported perovskite-based and Ru-based analogous electrocatalysts.

In the LSV curves of OER (**Figure 4d**), the potentials are recorded at a current density of 10 mA cm^{-2} ($E_{\text{OER},j=10}$) to evaluate the activity. LSMC-Ru delivers a much lower $E_{\text{OER},j=10}$ of 1.48 V vs. RHE as compared to the bare LSMC (1.7 V vs. RHE), and it also outperforms the benchmark RuO_2 (1.57 V vs. RHE). To further evaluate the intrinsic activity of the materials, the specific activity (SA) at overpotential of 300 mV is calculated based on the electrochemically active surface area (ECSA) (**Figure S11a-S11c**) and Brunauer–Emmett–Teller (BET) specific area (**Figure S12**). LSMC-Ru shows higher SA ($65.7 \mu\text{A cm}^{-2}_{\text{ECSA}}$, $144.3 \mu\text{A cm}^{-2}_{\text{BET}}$) than the bare LSMC ($4.0 \mu\text{A cm}^{-2}_{\text{ECSA}}$, $6.5 \mu\text{A cm}^{-2}_{\text{BET}}$), confirming the improved intrinsic activity resulting from the formation of the heterostructure. Besides, LSMC-Ru exhibits the lower Tafel slope (**Figure 4e**) of 87.3 mV dec^{-1} than the bare LSMC ($112.8 \text{ mV dec}^{-1}$) and RuO_2 ($117.2 \text{ mV dec}^{-1}$), implying the accelerated OER kinetics induced by the electronic interaction between LSMC and the anchored RuO_x . Electrochemical impedance spectra (EIS) (**Figure S11d**) show the decreased interfacial charge transfer resistance of LSMC-Ru compared with that of the bare LSMC, which also contributes to the superior electrochemical catalytic activity of LSMC-Ru. Furthermore, for the chronopotentiometry at 2 mA cm^{-2} (**Figure 4f**), LSMC-Ru shows a larger potential increasement (0.13 V) than the commercial RuO_2 (0.08 V) after 7 h test. It suggests that the OER stability of LSMC-Ru is not good enough, which requires further improvement in future studies.

Furthermore, CV tests (**Figure 4g**) are carried out to scrutinize the surface redox feature of the electrocatalysts. The bare LSMC shows no obvious redox peaks, indicating the relatively redox-inert surface that corresponds to the low electrochemical activity. In comparison, LSMC-Ru exhibits characteristic oxidation peaks at 0.64, 0.87, 1.07 vs. RHE, corresponding to the pseudocapacitive behavior of Mn (II/III), Mn (III/IV), Mn (II/IV), respectively,⁴³ which is consistent with the Mn-rich surface as evidenced by XPS (**Figure 1d**). Moreover, the small peak just anodic to the OER onset

could be assigned to the generation of high-valent Ru as the OER active sites.^{44,45} LSMC-Ru shows a lower peak potential at 1.28 V vs. RHE than the bare RuO₂ (1.33 V vs. RHE), indicating the lower barrier to form OER active sites. The CV peak shift confirms that the electron-deficient feature of Ru sites on LSMC-Ru is the key of the outstanding OER activity, which is consistent with the previous characterizations (XPS and EELS) and DFT simulation.

The potential gap between $E_{\text{ORR}, 1/2}$ and $E_{\text{OER}, j=10}$ is calculated to assess the bifunctional oxygen electrocatalytic activity of materials (**Figure 4h**). LSMC-Ru shows a potential gap of 0.72 V, which is comparable to the benchmark couple Pt/C+RuO₂ (0.73 V) and significantly lower than the bare LSMC (1.10 V). Additionally, $E_{\text{ORR}, 1/2}$ and $E_{\text{OER}, j=10}$ of the LSMC-Ru and other recently reported perovskite-based and noble metal-based electrocatalysts are compared in **Figure 4i**, further highlighting the superior bifunctional oxygen electrocatalytic activity of LSMC-Ru in this work.^{29,46-50}

2.4 The performance of Zn-air batteries

The LSMC-Ru bifunctional electrocatalyst is applied in an aqueous rechargeable ZAB. The air cathode is composed of three layers as shown in **Figure S13**, including a carbon-supported electrocatalyst layer, a gas diffusion layer, and a steel mesh acting as the current collector. LSMC-Ru shows an open circuit potential (**Figure S14**) of 1.43 V, which is close to the benchmark couple of Pt/C+RuO₂ (1.45 V). LSMC-Ru shows slightly lower discharge voltage and charge voltage than Pt/C+RuO₂ (**Figure 5a**), which is consistent with the OER and ORR activity tested on RDE (**Figure 4h**). Although the peak area power density (**Figure 5b**) of LSMC-Ru (159 mW cm⁻²) is lower than the of Pt/C+RuO₂ (206 mW cm⁻²), it is competitive to recently reported perovskite-based and Ru-based analogues (**Table S3**).^{11,12,15,29,51-53} Besides, the discharge profiles of the ZAB at different current densities from 1 to 30 mA cm⁻² (**Figure 5c**) show the good rate capability and fast dynamic response upon the current setting up and down, implying the potential application in automobiles.⁵⁴ The cycle stability of the ZAB is tested at 2 mA cm⁻² (**Figure 5d**). In the initial cycle, LSMC-Ru shows a charge-discharge voltage gap of 0.58 V, which is the same as that of Pt/C+RuO₂ (**Figure S15a**). After 200

cycles (**Figure S15b**), the voltage gap of LSMC-Ru increases to 1.05 V, and the increasement mainly comes from the charging voltage due to the decay of OER activity. It indicates that the insufficient OER stability of LSMC-Ru severely hinders the long-term cycle durability of the ZAB.

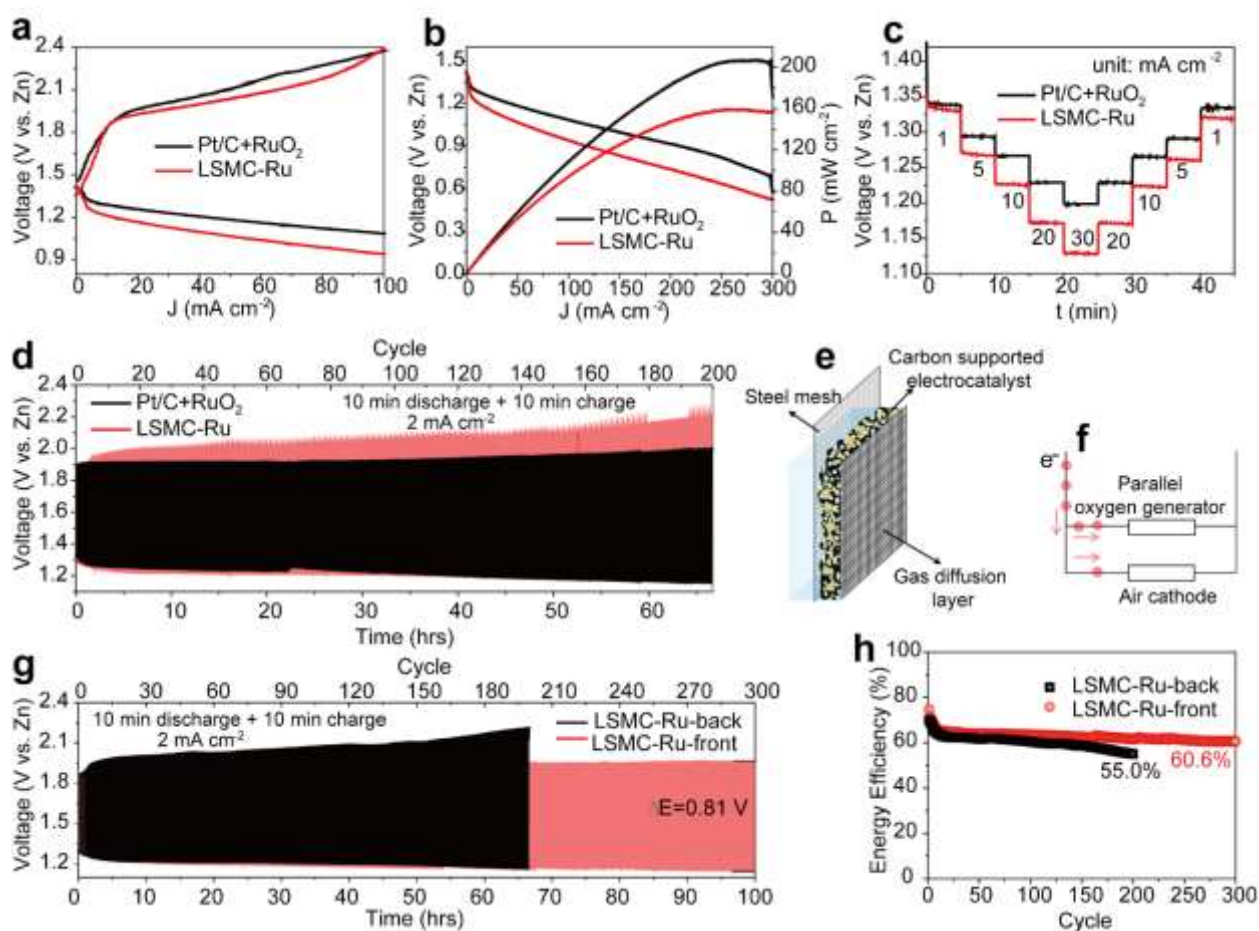


Figure 5. (a-d) Performance of aqueous ZABs using air cathodes with the back-contact steel mesh as shown in Figure S13. (a) Charge and discharge polarization curves, (b) discharge polarization curves (V-j) and power density curves (P-j), (c) rate capability test of discharge voltage at different current densities from 1 to 30 mA cm⁻², and (d) cycle stability tested at 2 mA cm⁻². (e) The schematic illustration of the front steel contact design for the air cathode. (f) Schematic illustration of the electron flow through the air cathode with the front-contacted steel as the parallel oxygen generator. A comparison of (g) the cycle stability and (h) energy efficiencies of the LSMC-Ru-assembled air cathodes with back and front steel contact.

To overcome the drawback of the OER stability of LSMC-Ru and fully exploit the ORR performance, we further engineered the structure of the air cathode. As suggested by Wang et al., a

nickel mesh in parallel with the air cathode could short the air cathode and afford the dominant OER current during the charging process, and thus avoid the oxidative degradation of the electrocatalyst layer⁵⁵. Accordingly, we optimized the air cathode structure by arranging the steel mesh in the front of the electrocatalyst layer (**Figure 5e**). Due to the lower resistance and higher hydrophilicity of the steel mesh as compared to the Nafion-rich and carbon-rich electrocatalyst layer, the OER current would tend to take place on the steel mesh more than in the electrocatalyst layer during the charging process. In this way, the steel mesh could simultaneously work as both the current collector and the oxygen generator to protect the electrocatalyst layer during the charging process (**Figure 5f**). The 200-mesh steel has ~ 80 μm space between the steel wires (**Figure S15c** inset), which guarantees the sufficient contact between the electrolyte and the catalyst layer. The air electrode with back and front steel mesh displays consistent discharge polarization curves for both LSMC-Ru and Pt/C+RuO₂ (**Figure S15c**), which indicates that the front steel contact design does not deteriorate the discharge performance of the battery. The galvanostatic charge-discharge curves at 2 mA cm^{-2} (**Figure S16**) shows that the air electrodes with back and front steel deliver the same discharge voltage. For the charging process, the LSMC-Ru-front electrode shows a Fe oxidation behavior at the initial stage of the first cycle, and then persists steady charging voltage platform corresponding to OER in the following cycles (**Figure S16**). For the long-term cycle stability at 2 mA cm^{-2} (**Figure 5g**), the LSMC-Ru-back electrode shows continuously increased charging voltage to 2.22 V after 200 cycles, whereas the LSMC-Ru-front electrode shows a relatively steady charging voltage of 1.95 V after 200 cycles (**Figure S15d**). The round-trip efficiency of LSMC-Ru-back decays to 55 % after 200 cycles, whereas LSMC-Ru-front preserves a much higher round-trip energy efficiency of 60.6 % after 300 cycles (**Figure 5h**). Besides, the electrode of Pt/C+RuO₂-front also shows increased cycle stability as compared to the electrode of Pt/C+RuO₂-back (**Figure S17**). The results indicate that the front steel contact is an efficient strategy to improve the cycle life of the air electrode.

3. Conclusions

In summary, an ultrafine RuO_x-anchored La_{0.8}Sr_{0.2}Mn_{0.5}Co_{0.5}O₃ (LSMC-Ru) is fabricated by a facile two-step process of solution treatment followed by annealing. The obtained LSMC-Ru realizes competitive cost and electrocatalytic activity by a low dosage (2.43 wt%) and high utilization of noble metal Ru. Superior bifunctional ORR and OER activity with a low potential gap of 0.72 V is achieved. The high activity can be attributed to the electron-rich Mn centers and electron-deficient Ru centers, which results from the selective cation leaching and the strong electronic interaction. The Zn-air battery using LSMC-Ru as the air electrode material delivers a high peak power density of 159 mW cm⁻² and a charge-discharge potential gap of 0.58 V at 2 mA cm⁻². Furthermore, a front steel contact design is proposed to alleviate the oxidative degradation of electrocatalyst layer in the air electrode, and it effectively elongates the cycle life of the ZAB, which persists a round-trip energy efficiency of 60.6 % after 300 cycles. This work provides simple and effective strategies for the design of bifunctional oxygen electrocatalysts and air electrodes, which could inspire the future development of high-performance and cost-effective metal-air batteries.

Acknowledgements

Y.W. Dai thanks the support by the PhD Fellowship of Research Grant Council, University Grant Committee, HK SAR. M. Ni thanks the support by Collaborative Research Fund (CRF) (Project No. C5031-20G) of Research Grant Council, University Grant Committee, HK SAR. We thank Professor Zijian Zheng from Institute of Textiles & Clothing of The Hong Kong Polytechnic University for the discussing and chemical support. We also thank Shiyanjia Lab (www.shiyanjia.com) for the help of characteriation in ICP, EDX-mapping, and EELS spectra.

Declaration of competing interests

The authors declare no conflict of interests.

CRedit authorship contribution statement

Yawen Dai: Investigation, Data curation, Formal Analysis, Writing - original draft. Jie Yu: Investigation, Writing - review & editing. Zhenbao Zhang: Formal Analysis, Software, Validation.

Shuo Zhai: Validation. Chun Cheng: Validation. Siyuan Zhao: Validation. Peng Tan: Formal analysis, Writing - review & editing. Zongping Shao: Writing - review & editing, Validation. Meng Ni: Funding acquisition, Project administration; Resources; Supervision, Writing - review & editing, Validation.

Supporting information description

Experimental section; photos of samples during synthesis; LSV curves of samples with varied Ru loading; XRD patterns; EDX spectra; the model for DFT calculation; calculation of ORR electron transfer numbers; CV curves for ECSA determination; N₂ adsorption-desorption curves; schematic illustration of the conventional three-layer air electrode structure; open circuit potential of Zn-air batteries; battery performance comparison of the air electrodes with front contact and back contact structure

References

- (1) Gu, P.; Zheng, M.; Zhao, Q.; Xiao, X.; Xue, H.; Pang, H. Rechargeable zinc–air batteries: a promising way to green energy. *J. Mater. Chem. A* **2017**, *5*, 7651-7666.
- (2) Tan, P.; Chen, B.; Xu, H.; Zhang, H.; Cai, W.; Ni, M.; Liu, M.; Shao, Z. Flexible Zn–and Li–air batteries: recent advances, challenges, and future perspectives. *Energy Environ. Sci.* **2017**, *10*, 2056-2080.
- (3) Zhang, W. D.; Hu, Q. T.; Wang, L. L.; Gao, J.; Zhu, H. Y.; Yan, X.; Gu, Z. G. In-situ generated Ni-MOF/LDH heterostructures with abundant phase interfaces for enhanced oxygen evolution reaction. *Appl. Catal., B* **2021**, *286*, 119906.
- (4) Fang, G.; Gao, J.; Lv, J.; Jia, H.; Li, H.; Liu, W.; Xie, G.; Chen, Z.; Huang, Y.; Yuan, Q. Multi-component nanoporous alloy/(oxy)hydroxide for bifunctional oxygen electrocatalysis and rechargeable Zn-air batteries. *Appl. Catal., B* **2020**, *268*, 118431.
- (5) Li, H.; Ma, L.; Han, C.; Wang, Z.; Liu, Z.; Tang, Z.; Zhi, C. Advanced rechargeable zinc-based batteries: Recent progress and future perspectives. *Nano Energy* **2019**, *62*, 550-587.
- (6) Shang, W.; Yu, W.; Liu, Y.; Li, R.; Dai, Y.; Cheng, C.; Tan, P.; Ni, M. Rechargeable alkaline zinc batteries: Progress and challenges. *Energy Stor. Mater.* **2020**, *31*, 44-57.
- (7) Tian, X.; Lu, X. F.; Xia, B. Y.; Lou, X. W. D. Advanced electrocatalysts for the oxygen reduction reaction in energy conversion technologies. *Joule* **2020**, *4*, 45-68.
- (8) Dai, Y.; Yu, J.; Ni, M.; Shao, Z. Rational design of spinel oxides as bifunctional oxygen

electrocatalysts for rechargeable Zn-air batteries. *Chem. Phys. Rev.* **2020**, *1*, 011303.

(9) Yu, W.; Shang, W.; Xiao, X.; Tan, P.; Chen, B.; Wu, Z.; Xu, H.; Ni, M. Achieving a stable zinc electrode with ultralong cycle life by implementing a flowing electrolyte. *J. Power Sources* **2020**, *453*, 227856.

(10) Wang, H. F.; Tang, C.; Zhang, Q. A review of precious-metal-free bifunctional oxygen electrocatalysts: rational design and applications in Zn-air batteries. *Adv. Funct. Mater.* **2018**, *28*, 1803329.

(11) Lu, Q.; Guo, Y.; Mao, P.; Liao, K.; Zou, X.; Dai, J.; Tan, P.; Ran, R.; Zhou, W.; Ni, M.; Shao, Z. Rich atomic interfaces between sub-1 nm RuO_x clusters and porous Co₃O₄ nanosheets boost oxygen electrocatalysis bifunctionality for advanced Zn-air batteries. *Energy Stor. Mater.* **2020**, *32*, 20-29.

(12) Wang, X.; Sunarso, J.; Lu, Q.; Zhou, Z.; Dai, J.; Guan, D.; Zhou, W.; Shao, Z. High-performance platinum-perovskite composite bifunctional oxygen electrocatalyst for rechargeable Zn-air battery. *Adv. Energy Mater.* **2020**, *10*, 1903271.

(13) Liang, X.; Shi, L.; Cao, R.; Wan, G.; Yan, W.; Chen, H.; Liu, Y.; Zou, X. Perovskite-Type Solid Solution Nano-Electrocatalysts Enable Simultaneously Enhanced Activity and Stability for Oxygen Evolution. *Adv. Mater.* **2020**, *32*, 2001430.

(14) Yu, J.; Wu, X.; Guan, D.; Hu, Z.; Weng, S.-C.; Sun, H.; Song, Y.; Ran, R.; Zhou, W.; Ni, M. Monoclinic SrIrO₃: an easily synthesized conductive perovskite oxide with outstanding performance for overall water splitting in alkaline solution. *Chem. Mater.* **2020**, *32*, 4509-4517.

(15) Chandrappa, S. G.; Moni, P.; Chen, D.; Karkera, G.; Prakasha, K. R.; Caruso, R. A.; Prakash, A. S. The influence of ruthenium substitution in LaCoO₃ towards bi-functional electrocatalytic activity for rechargeable Zn-air batteries. *J. Mater. Chem. A* **2020**, *8*, 20612-20620.

(16) Hu, C.; Hong, J.; Huang, J.; Chen, W.; Segre, C. U.; Suenaga, K.; Zhao, W.; Huang, F.; Wang, J. Surface decoration accelerates the hydrogen evolution kinetics of a perovskite oxide in alkaline solution. *Energy Environ. Sci.* **2020**, *13*, 4249-4257.

(17) Wang, Y.; Qian, G.; Xu, Q.; Zhang, H.; Shen, F.; Luo, L.; Yin, S. Industrially promising IrNi-FeNi₃ hybrid nanosheets for overall water splitting catalysis at large current density. *Appl. Catal., B* **2021**, *286*, 119881.

(18) Lv, G.; Wu, Y.; Wang, Y.; Kang, W.; Zhang, H.; Zhou, M.; Huang, Z.; Li, J.; Guo, Z.; Wang, Y. Rational design of perfect interface coupling to boost electrocatalytical oxygen reduction. *Nano Energy* **2020**, *76*, 105055.

(19) Ran, J.; Wang, T.; Zhang, J.; Liu, Y.; Xu, C.; Xi, S.; Gao, D. Modulation of Electronics of oxide perovskites by sulfur doping for electrocatalysis in rechargeable Zn-air batteries. *Chem. Mater.* **2020**, *32*, 3439-3446.

(20) Dai, Y.; Yu, J.; Cheng, C.; Tan, P.; Ni, M. Mini-review of perovskite oxides as oxygen electrocatalysts for rechargeable zinc-air batteries. *Chem. Eng. J.* **2020**, 125516.

(21) Yu, J.; Ran, R.; Zhong, Y.; Zhou, W.; Ni, M.; Shao, Z. Advances in porous perovskites:

synthesis and electrocatalytic performance in fuel cells and metal–air batteries. *Energy Environ. Mater.* **2020**, *3*, 121-145.

(22) Suntivich, J.; May, K. J.; Gasteiger, H. A.; Goodenough, J. B.; Shao-Horn, Y. A perovskite oxide optimized for oxygen evolution catalysis from molecular orbital principles. *Science* **2011**, *334*, 1383-1385.

(23) Dong, F.; Li, L.; Kong, Z.; Xu, X.; Zhang, Y.; Gao, Z.; Dongyang, B.; Ni, M.; Liu, Q.; Lin, Z. Materials Engineering in Perovskite for Optimized Oxygen Evolution Electrocatalysis in Alkaline Condition. *Small* **2020**, 2006638.

(24) Wang, X.; Pan, Z.; Chu, X.; Huang, K.; Cong, Y.; Cao, R.; Sarangi, R.; Li, L.; Li, G.; Feng, S. Atomic-scale insights into surface lattice oxygen activation at the spinel/perovskite interface of $\text{Co}_3\text{O}_4/\text{La}_{0.3}\text{Sr}_{0.7}\text{CoO}_3$. *Angew. Chem. Int. Ed.* **2019**, *131*, 11846-11851.

(25) Yu, J.; He, Q.; Yang, G.; Zhou, W.; Shao, Z.; Ni, M. Recent advances and prospective in ruthenium-based materials for electrochemical water splitting. *ACS Catal.* **2019**, *9*, 9973-10011.

(26) Suntivich, J.; Gasteiger, H. A.; Yabuuchi, N.; Nakanishi, H.; Goodenough, J. B.; Shao-Horn, Y. Design principles for oxygen-reduction activity on perovskite oxide catalysts for fuel cells and metal–air batteries. *Nat. Chem.* **2011**, *3*, 546-550.

(27) Wang, Q.; Xue, Y.; Sun, S.; Li, S.; Miao, H.; Liu, Z. $\text{La}_{0.8}\text{Sr}_{0.2}\text{Co}_{1-x}\text{Mn}_x\text{O}_3$ perovskites as efficient bi-functional cathode catalysts for rechargeable zinc-air batteries. *Electrochim. Acta* **2017**, *254*, 14-24.

(28) Du, X.; Ai, H.; Chen, M.; Liu, D.; Chen, S.; Wang, X.; Lo, K. H.; Pan, H. PLD-fabricated perovskite oxide nanofilm as efficient electrocatalyst with highly enhanced water oxidation performance. *Appl. Catal., B* **2020**, *272*, 119046.

(29) Seong, A.; Kim, J.; Kwon, O.; Jeong, H. Y.; Gorte, R. J.; Vohs, J. M.; Kim, G. Self-reconstructed interlayer derived by in-situ Mn diffusion from $\text{La}_{0.5}\text{Sr}_{0.5}\text{MnO}_3$ via atomic layer deposition for an efficient bi-functional electrocatalyst. *Nano Energy* **2020**, *71*, 104564.

(30) Yang, Y.; Mao, K.; Gao, S.; Huang, H.; Xia, G.; Lin, Z.; Jiang, P.; Wang, C.; Wang, H.; Chen, Q. A. M. O-, N-atoms-coordinated Mn cofactors within a graphene framework as bioinspired oxygen reduction reaction electrocatalysts. *Adv. Mater.* **2018**, *30*, 1801732.

(31) Li, J.; Chen, M.; Cullen, D. A.; Hwang, S.; Wang, M.; Li, B.; Liu, K.; Karakalos, S.; Lucero, M.; Zhang, H. Atomically dispersed manganese catalysts for oxygen reduction in proton-exchange membrane fuel cells. *Nat. Catal.* **2018**, *1*, 935-945.

(32) Yeo, B. S. Oxygen evolution by stabilized single Ru atoms. *Nat. Catal.* **2019**, *2*, 284-285.

(33) Liao, Y. Practical electron microscopy and database. *An Online Book* **2006**.

(34) Laffont, L.; Gibot, P. High resolution electron energy loss spectroscopy of manganese oxides: Application to Mn_3O_4 nanoparticles. *Mater. Charact.* **2010**, *61*, 1268-1273.

(35) Qian, D.; Xu, B.; Chi, M.; Meng, Y. S. Uncovering the roles of oxygen vacancies in cation migration in lithium excess layered oxides. *Phys. Chem. Chem. Phys.* **2014**, *16*, 14665-14668.

(36) Li, M.; Wang, H.; Zhu, W.; Li, W.; Wang, C.; Lu, X. RuNi nanoparticles embedded in N-

doped carbon nanofibers as a robust bifunctional catalyst for efficient overall water splitting. *Adv. Sci.* **2020**, *7*, 1901833.

(37) Liu, Y.; Ma, C.; Zhang, Q.; Wang, W.; Pan, P.; Gu, L.; Xu, D.; Bao, J.; Dai, Z. 2D electron gas and oxygen vacancy induced high oxygen evolution performances for advanced $\text{Co}_3\text{O}_4/\text{CeO}_2$ nanohybrids. *Adv. Mater.* **2019**, *31*, 1900062.

(38) Qiu, B.; Wang, C.; Zhang, N.; Cai, L.; Xiong, Y.; Chai, Y. CeO_2 -induced interfacial Co^{2+} octahedral sites and oxygen vacancies for water oxidation. *ACS Catal.* **2019**, *9*, 6484-6490.

(39) Feng, C.; Faheem, M. B.; Fu, J.; Xiao, Y.; Li, C.; Li, Y. Fe-based electrocatalysts for oxygen evolution reaction: progress and perspectives. *ACS Catal.* **2020**, *10*, 4019-4047.

(40) Lu, K.; Chang, G.; Zhang, H.; Yu, X. Y. Accelerating the oxygen evolution reaction kinetics of Co_3O_4 in neutral electrolyte by decorating RuO_2 . *Chem. Commun.* **2021**, *57*, 2907-2910.

(41) Yan, H.; Xie, Y.; Wu, A.; Cai, Z.; Wang, L.; Tian, C.; Zhang, X.; Fu, H. Anion-modulated HER and OER activities of 3D Ni-V-based interstitial compound heterojunctions for high-efficiency and stable overall water splitting. *Adv. Mater.* **2019**, *31*, 1901174.

(42) Gao, R.; Wang, J.; Huang, Z.-F.; Zhang, R.; Wang, W.; Pan, L.; Zhang, J.; Zhu, W.; Zhang, X.; Shi, C. Pt/ Fe_2O_3 with Pt-Fe pair sites as a catalyst for oxygen reduction with ultralow Pt loading. *Nat. Energy* **2021**, *6*, 614-623.

(43) Najafpour, M. M.; Moghaddam, N. J.; Hosseini, S. M.; Madadkhani, S.; Hołyńska, M.; Mehrabani, S.; Bagheri, R.; Song, Z. Nanolayered manganese oxides: insights from inorganic electrochemistry. *Catal. Sci. Technol.* **2017**, *7*, 3499-3510.

(44) Stoerzinger, K. A.; Rao, R. R.; Wang, X. R.; Hong, W. T.; Rouleau, C. M.; Shao-Horn, Y. The role of Ru redox in pH-dependent oxygen evolution on rutile ruthenium dioxide surfaces. *Chem* **2017**, *2*, 668-675.

(45) Stoerzinger, K. A.; Qiao, L.; Biegalski, M. D.; Shao-Horn, Y. Orientation-dependent oxygen evolution activities of rutile IrO_2 and RuO_2 . *J. Phys. Chem. L* **2014**, *5*, 1636-1641.

(46) Liu, S.; Sun, C.; Chen, J.; Xiao, J.; Luo, J.-L. A High-Performance Ruddlesden-Popper Perovskite for Bifunctional Oxygen Electrocatalysis. *ACS Catal.* **2020**, *10*, 13437-13444.

(47) Bu, Y.; Gwon, O.; Nam, G.; Jang, H.; Kim, S.; Zhong, Q.; Cho, J.; Kim, G. A highly efficient and robust cation ordered perovskite oxide as a bifunctional catalyst for rechargeable zinc-air batteries. *ACS Nano* **2017**, *11*, 11594-11601.

(48) Majee, R.; Islam, Q. A.; Bhattacharyya, S. Surface Charge Modulation of Perovskite Oxides at the Crystalline Junction with Layered Double Hydroxide for a Durable Rechargeable Zinc-Air Battery. *ACS Appl. Mater. Interfaces* **2019**, *11*, 35853-35862.

(49) Peng, S.; Han, X.; Li, L.; Chou, S.; Ji, D.; Huang, H.; Du, Y.; Liu, J.; Ramakrishna, S. Electronic and defective engineering of electrospun CaMnO_3 nanotubes for enhanced oxygen electrocatalysis in rechargeable zinc-air batteries. *Adv. Energy Mater.* **2018**, *8*, 1800612.

(50) Retuerto, M.; Calle-Vallejo, F.; Pascual, L.; Lumbeeck, G.; Fernandez-Diaz, M. T.; Croft, M.; Gopalakrishnan, J.; Pena, M. A.; Hadermann, J.; Greenblatt, M. $\text{La}_{1.5}\text{Sr}_{0.5}\text{NiMn}_{0.5}\text{Ru}_{0.5}\text{O}_6$ double

perovskite with enhanced ORR/OER bifunctional catalytic activity. *ACS Appl. Mater. Interfaces* **2019**, *11*, 21454-21464.

(51) Bian, J.; Su, R.; Yao, Y.; Wang, J.; Zhou, J.; Li, F.; Wang, Z. L.; Sun, C. Mg doped perovskite LaNiO₃ nanofibers as an efficient bifunctional catalyst for rechargeable zinc–air batteries. *ACS Appl. Energy Mater.* **2019**, *2*, 923-931.

(52) Gui, L.; Wang, Z.; Zhang, K.; He, B.; Liu, Y.; Zhou, W.; Xu, J.; Wang, Q.; Zhao, L. Oxygen vacancies-rich Ce_{0.9}Gd_{0.1}O_{2-δ} decorated Pr_{0.5}Ba_{0.5}CoO_{3-δ} bifunctional catalyst for efficient and long-lasting rechargeable Zn-air batteries. *Appl. Catal., B* **2020**, *266*, 118656.

(53) Arafat, Y.; Azhar, M. R.; Zhong, Y.; Xu, X.; Tadé, M. O.; Shao, Z. A Porous Nano-Micro-Composite as a High-Performance Bi-Functional Air Electrode with Remarkable Stability for Rechargeable Zinc–Air Batteries. *Nanomicro Lett.* **2020**, *12*, 1-16.

(54) Yang, D.; Zhang, L.; Yan, X.; Yao, X. Recent progress in oxygen electrocatalysts for zinc–air batteries. *Small Methods* **2017**, *1*, 1700209.

(55) Wang, K.; Liao, C.; Wang, W.; Xiao, Y.; Liu, X.; Zhao, S. Physical shortcut accelerating electron transport of rechargeable zinc-air battery. *Mater. Today Energy* **2019**, *14*, 100340.

Graphic abstract

